Chemical Engineering Journal 495 (2024) 153315

Contents lists available at ScienceDirect

Chemical Engineering Journal

journal homepage: www.elsevier.com/locate/cej

Metal-Organic framework incorporated luminescent PTCA combined with novel co-reactant accelerator for ultra-sensitive electrochemiluminescence detection of CA19-9

Haiyang Li [a], Mingyue Shao [a], Jinglong Fang [a], Yuyang Li [a], Xiaojun Sun [a], Xiang Ren [a], Qin Wei [a,b,*], Huangxian Ju [a,c], Hongmin Ma [a,*]

[a] Key Laboratory of Interfacial Reaction & Sensing Analysis in Universities of Shandong, School of Chemistry and Chemical Engineering, University of Jinan, Jinan 250022, PR China
[b] Department of Chemistry, Sungkyunkwan University, Suwon 16419, Republic of Korea
[c] State Key Laboratory of Analytical Chemistry for Life Science, School of Chemistry and Chemical Engineering, Nanjing University, Nanjing 210023, PR China

ARTICLE INFO

Keywords:
Electrochemiluminescence
Aggregation-caused quenching
PTCA
Metal–organic frameworks
CA19-9
Co-reaction accelerator

ABSTRACT

Polycyclic aromatic hydrocarbons (PAHs) are commonly used as electrochemiluminescence (ECL) luminophores. However, PAHs are limited by the aggregation-caused quenching (ACQ) effect, which reduces ECL emission. Therefore, developing an ECL system from PAHs with efficient luminescence is a significant challenge. In this work, a two-ligand strategy was proposed to assemble 3, 4, 9, 10-perylenetetracarboxylic acid (PTCA) into zeolitic imidazole framework-8 (ZIF-8). The ACQ effect of PTCA was inhibited by participating in the formation of metal–organic frameworks (MOFs) and a luminescent ZIF-8-PTC (Z8P) composite was obtained. Satisfactorily, conceptual experiments demonstrated that the significantly higher ECL efficiency of Z8P was achieved compared with PTCA monomers and aggregates. On the sensing substrate, a novel co-reactant accelerator (Au@MFNC) was used to achieve continuous catalysis of the persulfate ($K_2S_2O_8$) with the Prussian blue analogues (PBAs) as a template under the efficient synergistic effect of MoS_2. Through the reversible transformation of the transition metal valence states, a sufficient amount of sulfate radicals ($SO_4^{\bullet-}$), again amplifying the ECL signal of Pd@Z8P. Under ideal conditions, the constructed dual-MOFs ECL immunosensor had a wide response range ($1 \times 10^{-4} - 1 \times 10^{2}$ U/mL) and a low limit of detection (LOD) (6×10^{-5} U/mL), which provided an alternative method for CA19-9 ultrasensitive detection, and broadened a new idea for the development of high-performance luminescent MOFs.

1. Introduction

Electrochemiluminescence (ECL) possesses the significant advantages of high sensitivity, spatial and temporal controllability, low background signal, is widely used in immunoassay and environmental testing [1–4]. Presently, ECL development is focused on the construction of novel luminophores to enhance the speedy signal response of the sensors [5–8]. 3, 4, 9, 10-perylenetetracarboxylicacid (PTCA), a classic polycyclic aromatic hydrocarbon (PAH), is often used for luminophores in the field of ECL due to its good structural stability and excellent quantum yield [9]. It is noted that most PAHs and their derivatives would be prone to aggregation-caused quenching (ACQ) effect in the aqueous phase due to the π-π stacking of their aromatic rings [10]. To overcome the above difficulties, manifold strategies have been successively reported. Tang's team covalently linked distorted aggregation-induced emission (AIE) molecules to planar PAHs molecules, which inhibited the π-π stacking of PAHs, and realized the transition from the ACQ effect to the AIE effect [11]. Bai et al. developed a metallized porphyrin hybrid (LPH) using the solvothermal reaction of the polycyclic aromatic hydrocarbon molecule (TCPP) with the metal lanthanum, overcoming the shortcomings of instability and easy aggregation of TCPP [12]. Moreover, the co-assembly of luminophores as second ligands into metal–organic frameworks (MOFs) is also an efficacious strategy worth exploring. Zeolitic imidazole framework-8 (ZIF-

* Corresponding authors at: Key Laboratory of Interfacial Reaction & Sensing Analysis in Universities of Shandong, School of Chemistry and Chemical Engineering, University of Jinan, Jinan 250022, PR China (Qin Wei).
E-mail addresses: sdjndxwq@163.com (Q. Wei), chm_mahm@ujn.edu.cn (H. Ma).

https://doi.org/10.1016/j.cej.2024.153315
Received 14 April 2024; Received in revised form 8 June 2024; Accepted 18 June 2024
Available online 21 June 2024

8) is a classical porous crystalline material formed by the coordination of zinc ions (Zn^{2+}) with the conventional ligand 2-methylimidazole (2-MI) [13,14]. Due to its abundant metal content, superior water stability and well-ordered pore structure, it can be used as a nanoreactor for co-assembly with ECL luminophores to improve ECL efficiency and stability [15,16]. Based on the above considerations, we carefully selected the luminescent PTCA ligand to co-assemble with the 2-MI as the luminescent ZIF-8-PTC (Z8P), which retained the native advantage of ZIF-8, but also enlarged the distance between the perylene rings and successfully weakened the ACQ effect of PTCA.

The sensing substrate plays a crucial role in the ECL system in building high performance sensors [17,18]. Obviously, substrates with co-reaction accelerator effects are more interesting. The persulfate ($K_2S_2O_8$) as a sacrificial additive in the ECL system, a massive consumption is not sufficient for a stable output of the ECL signal, and the emergence of co-reaction accelerators has aptly compensated for the above drawbacks. For examples, Yuan's team introduced co-reactant accelerators into ECL systems for the first time, pioneering ternary sandwich immunosensors containing luminophores, co-reactants and co-reactant accelerators [19]. Willner et al. designed three Prussian blue analogues, CuFe, FeCo and FeCoFe, to be used as peroxidase-like enzymes to enhance the chemiluminescence of the luminol-H_2O_2 system [20]. It is evident that Prussian blue analogues (PBAs), a common MOFs, have a well-founded research basis and application prospect as co-reactant accelerators with variable valence metal [21].

Pancreatic cancer (PC), as a common malignant tumor in the digestive tract, has the title of "king of cancers" and has a mortality rate of 80 % [22,23]. Carbohydrate antigen 19-9 (CA19-9), a Lewis antigen expressed by type I transmembrane glycoprotein (MUC1), serves as a specific tumor marker for PC [24], as well as being an important marker indicative of the risk of having gastric (GC), colorectal (CRC), and uroepithelial (UC) cancers [25–27]. Consequently, the integration of ECL technology for the sensitive detection of CA19-9 is of significant importance for the early diagnosis and prognosis of treatment for PC.

In this work, the luminescent ligand (PTCA) and the conventional ligand (2-MI) were chosen as dual-ligands to synthesize Z8P with ECL-active, relying on the ordered assembly within ZIF-8, thus eliminating the ACQ effect of PTCA. In situ formation of palladium nanoparticles (Pd NPs) on the surface of Z8P accelerated the electron transport rate of the luminophores while ensuring a tight binding to the secondary antibody (Ab_2) to improve the sensitivity of the immunosensor (Scheme 1A). For the sensor substrate, FeNiCo-PBAs (FNC) nanocubes were prepared by co-precipitation using sodium citrate as a templating agent, followed by enveloping MoS_2 nanoflakes on their surface, which on the one hand increased the electrochemcial active surface area, and on the other hand prevented aggregation phenomena between the nanocubes. Secondly, gold nanoparticles (Au NPs) were bound on the surface of MoS_2/FeNiCo-PBAs (MFNC) with Au−S bonds, which acted as a bridge between the primary antibody (Ab_1), and enhanced the conductivity of MFNC (Scheme 1B). Finally, in Scheme 1C, Au@MoS_2/FeNiCo-PBAs (Au@MFNC) acted as co-reactant accelerators in the presence of variable valence transition metals, to achieve sustained catalysis of $K_2S_2O_8$

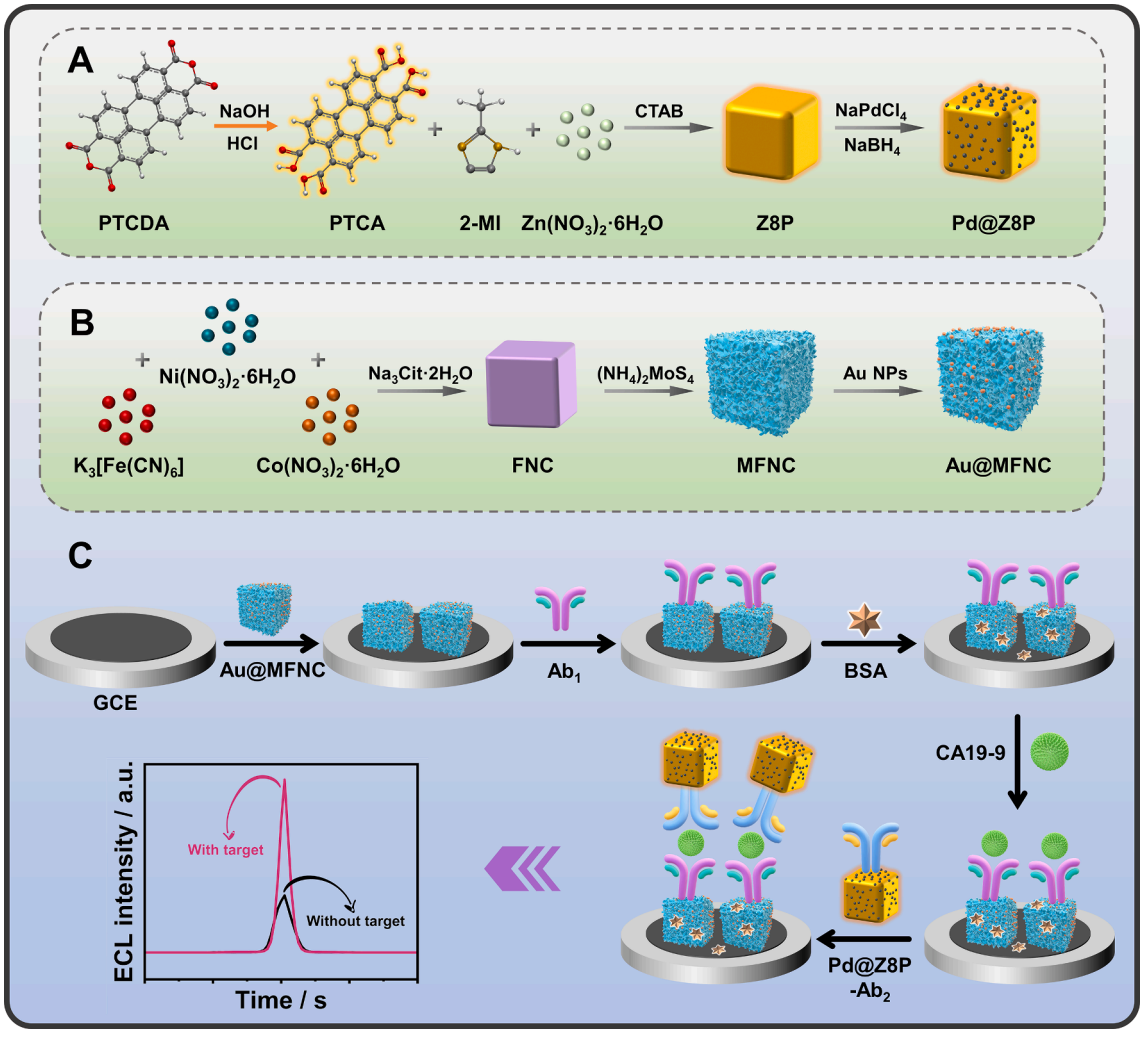

Scheme 1. (A) Schematic presentation of preparation of Pd@Z8P, (B) Au@MFNC and (C) fabrication process of the ECL immunosensor.

through reversible transformation of valence states to satisfy the $SO_4^{\bullet-}$ required for the luminophores, in order to once again enhance the ECL signals of Pd@Z8P. Based on the above sensor components, the dual-MOFs sandwich-type ECL immunosensor was successfully fabricated to realize the ultrasensitive detection of CA19-9. In particular, the co-assembly of PAH derivatives with conventional ligands into MOFs is the key to alleviate the ACQ effect of PAHs, providing a new strategy for exploring efficient ECL luminophores and constructing ultrasensitive ECL immunosensors.

2. Experimental section

2.1. Materials and apparatus

All the materials and apparatus can be found in the Supplementary Material.

2.2. Preparation of Au@MFNC

The MFNC were synthesized based on previous work with slight modifications [28]. The prepared 30 mg FNC and 10 mg $(NH_4)_2MoS_4$ were dissolved in 30 mL DMF and stirred for 15 min. The mixture was then transferred to a 50 mL Teflon-lined stainless-steel autoclave and reacted at 210 °C for 20 h. The black precipitate obtained was centrifuged at 7000 rpm for 5 min and washed alternately with ultrapure water and EtOH. Finally, the obtained MFNC were dried at 60 °C overnight for further use. The preparation of bare MoS_2 nanoflakes was similar to the above method, except for the addition of FNC.

The synthesized 5 mL Au NPs was dissolved in 10 mL MFNC (1 mg/mL) aqueous solution with continuous stirring for 12 h to ensure that the Au NPs were sufficiently immobilized on the surface of the MFNC through Au−S bonds. The final product was centrifuged at 9000 rpm for 10 min and washed alternately with ultrapure water and EtOH. Finally, it was dried at 60 °C overnight for further use. The preparation process of Au NPs and FNC can be obtained from the Supplementary Material.

2.3. Preparation of Pd@Z8P

Firstly, 2 mg PTCA and 10 mg CTAB were dissolved in 1 mL DMF and stirred for 5 min, then added to 17.5 mL ultrapure water (containing 790 mM 2-MI) and continued to stir for 5 min. Finally, 2.5 mL Zn $(NO_3)_2{\cdot}6H_2O$ (97.5 mM) solution was added. The mixed solution was stirred at RT for 3 h and left to stand for 6 h. The synthesized Z8P was centrifuged at 10000 rpm for 10 min, washed with ultrapure water and dried at 60 °C overnight for further use.

50 mg Z8P was dissolved in 5 mL ultrapure water and dispersed by ultrasonication for 5 min. Then 5 mL Na_2PdCl_4 (1 mg/mL) aqueous solution was added, and ultrasonication was continued for 5 min, with stirring for 30 min at RT. Finally, 1 mL fresh $NaBH_4$ (0.1 M) aqueous solution was rapidly injected under vigorous stirring. The Pd@Z8P was collected after continued stirring for 30 min. The final product was centrifuged at 10000 rpm for 10 min, washed with ultrapure water and dried at 60 °C overnight for further use. The preparation process of PTCA and ZIF-8 can be obtained from the Supplementary material.

2.4. Preparation of Pd@Z8P-Ab_2 bioconjugates

2 mg Pd@Z8P and 800 μL PBS (1/15 M, pH 7.4) and 200 μL Ab_2 (10 μg/mL) were well-stirred and incubated for 12 h at 4 °C, then centrifugated at 12000 rpm for 10 min and washed with PBS (1/15 M, pH 7.4). To seal the nonspecific active site on the surface of Pd@Z8P, 800 μL PBS (1/15 M, pH 7.4) and 200 μL BSA (1 wt%) were thoroughly mixed with the above product and shaken at 4 °C for 12 h. Then, the incubated bioconjugates were centrifuged at 12000 rpm for 10 min to remove the supernatant. Finally, the centrifuged precipitate was dispersed in 1 mL PBS (1/15 M, pH 7.4) and stored at 4° C for further use.

2.5. Construction of ECL immunosensor

Firstly, the glassy carbon electrode (GCE) was pretreated with Al_2O_3, ultrasonically cleaned with ultrapure water and EtOH, and blown dry with N_2. Then 10 μL Au@MFNC (3 mg/mL) was added dropwise to the GCE surface. Then, 10 μL Ab_1 and 5 μL BSA (1 wt%) were sequentially added dropwise to the modified GCE at 4 °C and incubated for 12 h. 5 μL different concentrations of CA19-9 were added dropwise to the surface of the electrodes and incubated for 2 h at 4 °C. Finally, 10 μL Ab_2-Pd@Z8P was added dropwise to the surface of the modified electrode, and the immunosensor was fully constructed and stored at 4 °C for subsequent detection. It should be noted that after each step, the GCE surface needed to be rinsed with PBS (1/15 M, pH 7.4) to remove unbound reagents.

2.6. ECL test for CA19-9

The test of ECL signals was performed in a three-electrode system. The electrolyte was 10 mL PBS (1/15 M, pH 7.4, containing 74.65 mM $S_2O_8^{2-}$). The test parameters were as follows: the voltage scanning range was 0 to − 1.5 V, the photomultiplier tube voltage was 500 V, and the scanning rate was 0.2 V/s.

3. Results and discussion

3.1. Characterization of Pd@Z8P

The morphology of Z8P, Pd@Z8P was characterized by scanning electron microscopy (SEM) and transmission electron microscopy (TEM). In Fig. 1A and Fig. 1B, Z8P had a uniformly arranged cubic structure with an average size of about 60 nm. However, it was reported that PTCA was rod-shaped and poorly dispersed, indicating that the addition of PTCA did not change the original morphology of ZIF-8 [29,30]. As shown in Fig. 1C, the uniform loading of Pd NPs on the surface of Z8P can be clearly seen to ensure further tight connection with the antibody. In addition, the crystal structure of Pd@Z8P was determined by X-ray powder diffraction (XRD). In Fig. 1D, the XRD pattern of Pd@Z8P maintained consistency with the characteristic peaks in the simulated XRD pattern (CCDC 864309) [29], indicating that the synthesized Pd@Z8P possessed favorable crystallinity. By comparing the XRD patterns of Z8P and ZIF-8, no XRD characteristic peaks of other substances, such as PTCA, were observed, suggesting that PTCA might be involved in the coordination within the framework of ZIF-8. In Fig. S1, the Fourier transform infrared (FT-IR) spectra of PTCA (curve a) showed four characteristic bands of 2557, 1687, 1385, and 1287 cm^{-1}, corresponding to the O−H and C=O bonds stretches in −COOH, and the C=O and C−O−C bonds stretches in the benzene ring, respectively [9]. Notably, the observation of the FT-IR spectra of Z8P revealed the disappearance of the characteristic bands at 2557 and 1687 cm^{-1} was found, demonstrating the coordination between $-COO^-$ of PTCA and Zr^{4+} [31].

Meanwhile, X-ray photoelectron spectroscopy (XPS) was used to measure the surface elemental composition, chemical states and bonds information of Pd@Z8P. Fig. S2 showed the XPS survey spectra of C 1s, O 1s, N 1s, Zn 2p and Pd 3d of Pd@Z8P, reflecting the coexistence of five elements in the hybrids. Deconvolution of the C 1s peak (Fig. 1E) showed three binding energies at approximately 284.8, 285.6 and 286.6 eV, which corresponded to C−C / C=C, C−N / C=N and C−O / C=O bonds, respectively [32]. Deconvolution of the O 1s peak (Fig. 1F) showed three peaks at about 528.8, 531.0 and 534.3 eV corresponding to Zn−O, C−O and C=O bonds, respectively [33]. In addition, in the N 1s spectrum (Fig. 1G), there were three binding energy peaks at 398.2, 398.9 and 400.3 eV corresponding to the XPS signals of pyridinic−N, Zn−N and pyrrolic−N bonds, respectively [34]. In the Zn 2p spectrum (Fig. 1H), it could be found that two binding energy peaks around 1021.3 and 1044.4 eV attributed to Zn^{2+} $2p_{3/2}$ and Zn^{2+} $2p_{1/2}$,

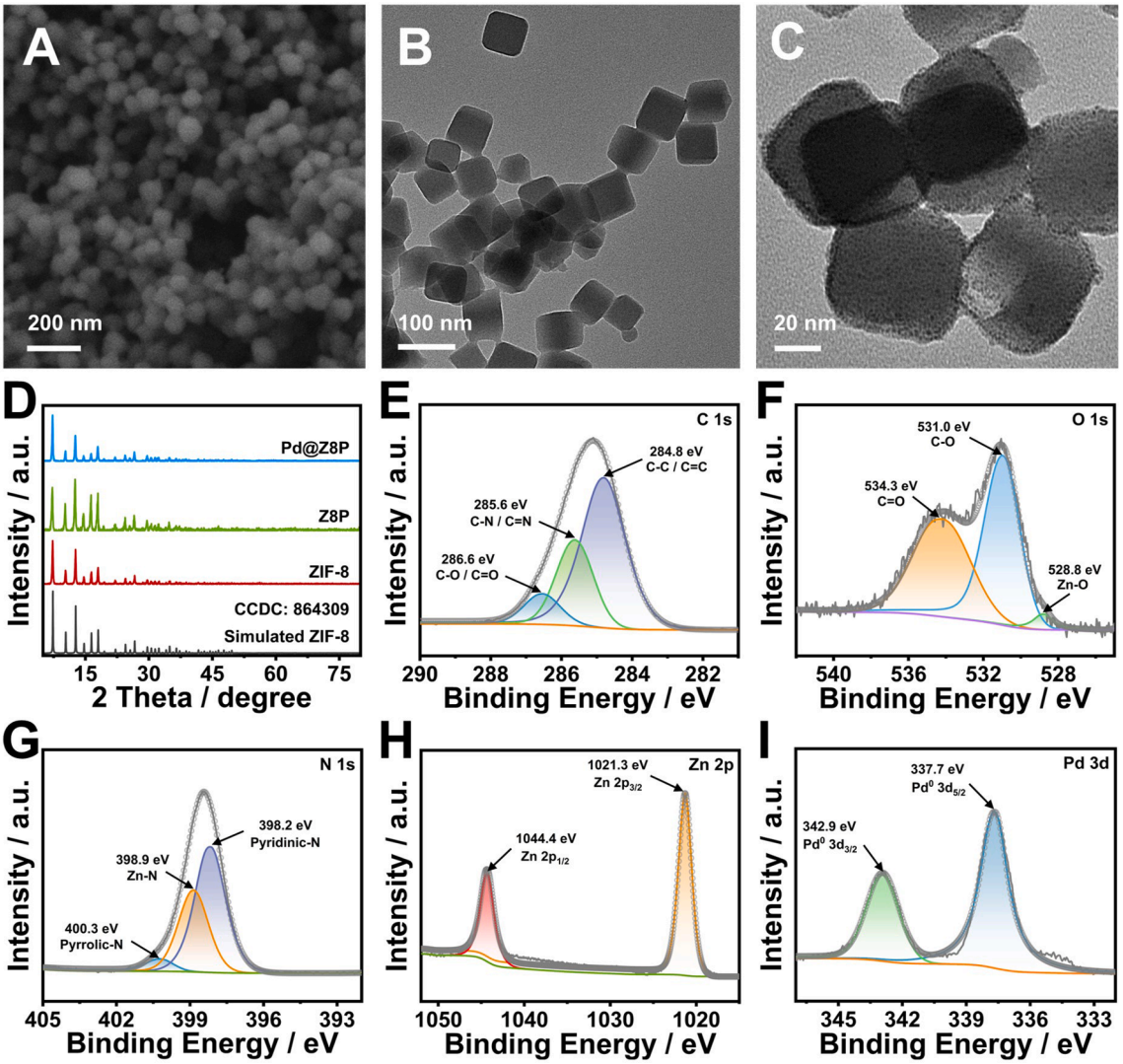

Fig. 1. (A) SEM image of Z8P. (B) TEM images of Z8P and (C) Pd@Z8P. (D) XRD patterns of ZIF-8, Z8P and Pd@Z8P. (E) XPS spectra of C 1s, (F) O 1s, (G) N 1s, (H) Zn 2p and (I) Pd 3d for Pd@Z8P.

respectively, indicating the presence of the Pd@Z8P central metal ion. Meanwhile, in the Pd 3d spectrum of Fig. 1I, considering a spin–orbit separation of about 5.2 eV, Pd 3d was resolved into two peaks [35]. The binding energy of the double peaks corresponded to 337.7 eV for Pd $3d_{5/2}$ and 342.9 eV for Pd $3d_{3/2}$ in the metal Pd^0 state, clearly indicating the efficient reduction efficiency of the Pd precursor (Na_2PdCl_4) [36]. Finally, the absorption peaks of ZIF-8, PTCA and Z8P were analyzed by ultraviolet–visible absorption spectroscopy (UV-vis) (Fig. S3), and ZIF-8 did not have any absorption peaks in the range of 330 − 360 nm, whereas strong absorption peaks existed at 473 nm and 517 nm for PTCA. Comparing the absorption spectra of Z8P, the intense absorption peak at 473 nm remained almost unchanged, while the weaker absorption peak at 517 nm disappeared and a new peak appears at 444 nm. This transition might be due to the increased electron-donor ability of the substituent PTCA and the presence of strong molecular interactions within Z8P [12]. All of the above characterizations provide convincing evidence for the successful preparation of Pd@Z8P hybrids.

3.2. Luminescence performance of Z8P

The luminescence performance of Z8P was characterized via ECL emission spectra and photoluminescence (PL) spectra. In Fig. 2A, the 3D ECL-wavelength-potential image demonstrated the ECL emission evolutionary process of the Z8P (scanning potentials from 0 V to − 1.5 V). Meanwhile, it was clearly showed from the ECL 2D planar heat image of Z8P (Fig. 2B) that Z8P had the strongest ECL emission at about 559 nm. After measuring the optimal excitation wavelength of 480 nm (Fig. S4), the PL emission spectra of Z8P was obtained with the optimal PL emission wavelength of 554 nm. Secondly, ECL spectra scanning was performed with a central wavelength of 500 nm, and the ECL emission spectra of Z8P was obtained. The optimal ECL emission wavelength was 559 nm, which was consistent with the above results. In Fig. 2C, it was noted that the PL emission wavelength was very close to the ECL emission wavelength, indicating that the Z8P/$S_2O_8^{2-}$ system belonged to the non-surface state ECL emission, and also indicating that ECL and PL emission undergo similar processes of excited state, ground state and light state emission [37]. The effects of apparatus during the test may account for subtle differences [10]. Finally, to observe the luminescence performance of Z8P more intuitively (Fig. 2D), a confocal laser scanning microscope (CLSM) was used at an excitation wavelength of 488 nm, and Z8P emitted a bright fluorescence (rendered in yellow). The inset of Fig. 2D showed a fluorescence photograph of the solid powder of Z8P irradiated under dark conditions with a UV lamp (365 nm excitation).

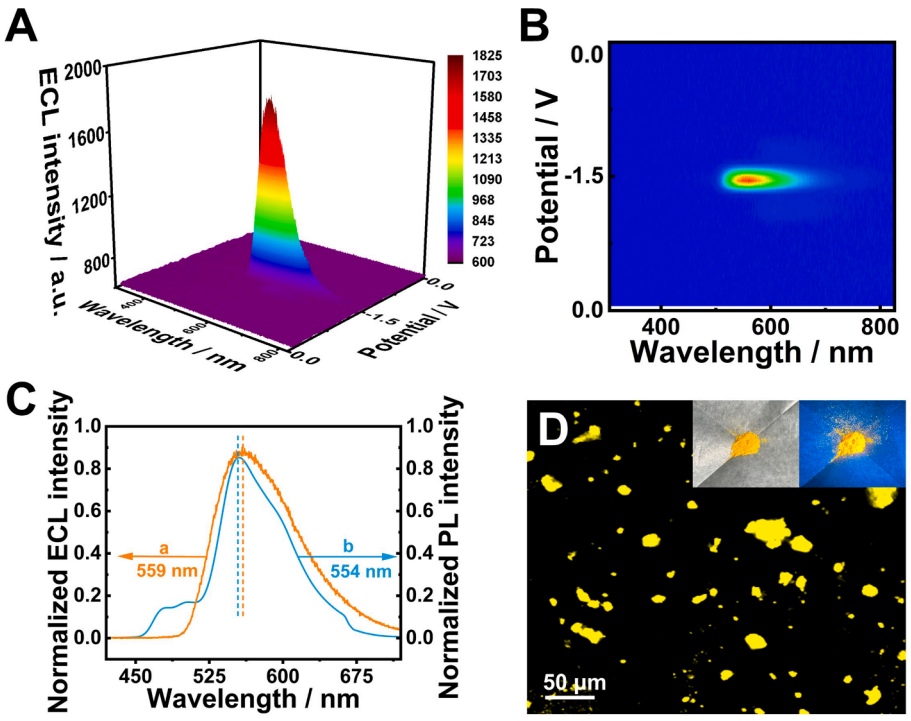

Fig. 2. (A) 3D ECL-wavelength-potential image and (B) 2D planar heat image of Z8P in PBS (1/15 M, pH 7.4 with 80 mM $S_2O_8^{2-}$). (C) ECL (a) and PL (b) emission spectra of Z8P. (D) Fluorescence microscopic image of Z8P (The insets are photos of solid powders irradiated with and without 365 nm excitation).

3.3. ECL and PL enhancement of Z8P

To demonstrate the feasibility of the luminescence enhancing strategy for Z8P, the PL properties of PTCA in mixed solvent were first investigated. In Fig. S5, PTCA exhibited strong PL emission in dilute solution of DMF, and the PL intensity gradually decreased with the increase of H_2O/DMF (volume ratio), indicating that PTCA was a typical ACQ molecule. In Fig. 3, ECL and PL tests were performed on PTCA aggregates, PTCA monomers and Z8P under the same conditions. The monomers showed significantly enhanced PL intensity compared to the aggregates, further demonstrating that PTCA had an ACQ effect in the aqueous phase (Fig. 3A). The PL intensity of Z8P (855.7 a.u.) was about 2.2 and 5.3 times higher than that of PTCA monomers (386.5 a.u.) and PTCA aggregates (162.1 a.u.), respectively, providing preliminary evidence for the feasibility of the proposed strategy. The inset of Fig. 3A showed the fluorescence photograph of the three substances under dark conditions (365 nm excitation), and it was clear that the best PL intensity was seen for Z8P. As shown in Fig. 3B, the ECL intensity of both PTCA monomers and aggregates weakened with the increase of the number of cyclic scans, attributed to the leakage of PTCA on the electrode surface. However, Z8P showed excellent stability with an RSD of only 0.74%, indicating that the immobilization of PTCA in ZIF-8 weakened the ACQ effect and prepared high-performance ECL luminophores. Finally, the proposed strategy was further validated by calculating the relative ECL efficiency (Φ_{ECL}). Using the $[Ru(bpy)_3]^{2+}/S_2O_8^{2-}$ system was taken as a standard ($\Phi_{st} = 5\%$), the calculated relative ECL efficiency for the Z8P/$S_2O_8^{2-}$ system was 9.35%, which was higher than that of PTCA monomers ($\Phi_m = 4.35\%$) and PTCA aggregates ($\Phi_a = 2.06\%$) (the Eq. (S1) was shown in the Supplementary Material). Summarizing the above discussion, the reasons for the enhanced luminescence of Z8P were as follows: (1) PTCA and 2-MI acted as an intermediate ligand to assemble Z8P, and the distance between the perylene rings in PTC was amplified in MOF, which suppressed π-π stacking, overcame the ACQ effect. (2) Since Z8P possessed the advantages of cubic structure, large specific surface area and high porosity, a large number of PTC luminophores were stored inside and on the surface. (3) The pore of Z8P were enriched with a large amount of $S_2O_8^{2-}$, which shortened the electron transfer distance between the

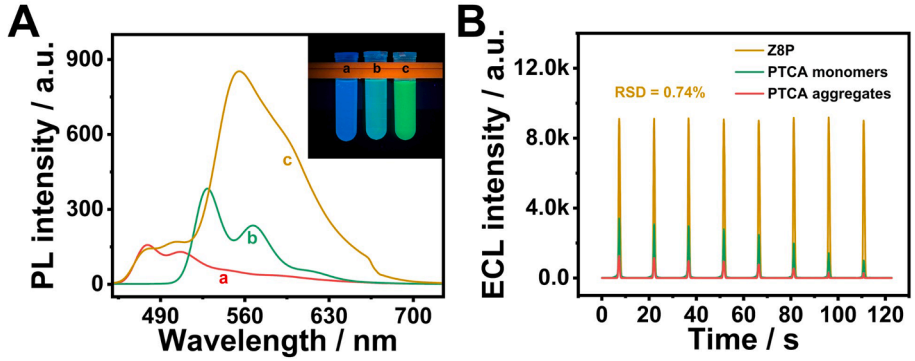

Fig. 3. (A) PL intensity of 0.1 mM PTCA (aggregates) in PBS (1/15 M, pH 7.4) (a), 0.1 mM PTCA (monomers) in DMF (b) and Z8P containing 0.1 mM PTC in PBS (1/15 M, pH 7.4) (c) (The inset is a photo of the three corresponding solutions irradiated with 365 nm excitation). (B) ECL intensity of 0.1 mM PTCA in PBS (1/15 M, pH 7.4 with 80 mM $S_2O_8^{2-}$), in DMF (with 80 mM $TBAPF_6$) and Z8P including 0.1 mM PTC in PBS (1/15 M, pH 7.4 with 80 mM $S_2O_8^{2-}$).

luminophores and active intermediates, and facilitated more luminophores to be electrochemically excited. Therefore, the synthesis of ECL-active MOFs by a dual-ligand strategy is an effective approach to overcome the ACQ effect of PAHs and improve the ECL efficiency.

3.4. Characterization of Au@MFNC

Firstly, FNC nanocubes were synthesized by co-precipitation. In Fig. 4A, the FNC had smooth surfaces and well dispersed with average sizes between 200 − 300 nm. The nanocube was used as a template to grow MoS_2, and the morphology was shown in Fig. 4B. The surface of MFNC appeared wrinkled without agglomeration, and the Fig. 4C showed even more clearly that the surface of FNC was encapsulated by MoS_2 nanosheets. In Fig. 4D, we zoomed in to observe a corner of the MFNC cube, which clearly showed the ultrathin features of the MoS_2 nanosheets, with a vertical height of about 20 nm and a thickness of a few nanometers on the surface of the FNC. Secondly, the Au NPs were uniformly loaded on the MFNC (Fig. 4E). Meanwhile, we tested the Zeta-potentials (ζ) of FNC, Au NPs and Au@MFNC. In Fig. S6, the Zeta-potential of FNC was − 25.9 mV, after binding with Au NPs (ζ = − 14.8 mV), the potential of Au@MFNC (ζ = − 34.4 mV) decreased again, further indicating that the Au NPs were successfully anchored on the surface of MFNC via Au−S bonds. Finally, by Energy Dispersive X-ray spectroscopy (EDS) elemental mapping (Fig. 4F) and EDS spectrum (Fig. S7), it was illustrated that the elements of Fe, Ni, Co, Mo, S and Au were uniformly distributed in the nanocubes. We investigated the crystal structures of the above materials (Fig. 4G), and the XRD diffraction peaks of FNC matched well with the standard patterns of FeNi-PBAs (JCPDS 51-1897) and CoFe-PBAs (JCPDS 80-2395) [38]. By analyzing the XRD pattern of MFNC and comparing the XRD pattern of the prepared pure MoS_2, in addition to the XRD characteristic peaks of FNC, new diffraction peaks appeared at 9° and 33°, indicating that MFNC were successfully prepared. Interestingly, the XRD patterns of prepared MoS_2 and MFNC were compared with the standard XRD pattern of MoS_2 (JCPDS 75-1539), and it was found that the corresponding (0 0 2) crystal plane disappeared at 14°, while a sharp diffraction peak appeared at 9°. This was attributed to the fact that the MoS_2 prepared by the solvothermal reaction of $(NH_4)_2MoS_4$ was not a stacked structure but consists of monolayer or multilayer MoS_2 nanosheets [39].

3.5. Signal amplification mechanism

Firstly, the ECL signals of different materials were tested in PBS (1/15 M, pH 7.4, with $S_2O_8^{2-}$). In Fig. 5A, the ECL intensity of the bare GCE was weak (631.5 a.u., curve a), and the signal originated from the emission of ($^1(O_2)_2$*) [40]. After modification of Pd@Z8P on the GCE (curve b), a significant ECL signal (5672.3 a.u.) appeared, which was attributed to the ECL response between $S_2O_8^{2-}$ and Pd@Z8P. The introduction of Pd NPs accelerated the electron transfer rate of Z8P to a certain extent while improving the luminescence performance of Z8P (Fig. S9), thus increasing the sensitivity of the immunosensor. After further modification by FNC (curve c), the ECL signal was enhanced (9520.4 a.u.), suggesting that FNC played a key role in catalyzing the production of $SO_4^{\bullet-}$ from $S_2O_8^{2-}$. When replacing with Au@MFNC (curve d), the ECL intensity was elevated to 12405.8 a.u., and it can be seen that the signal was amplified again, attributed to the efficient synergistic catalysis of MoS_2. Meanwhile, there was essentially no ECL emission when Pd@Z8P and Pd@Z8P + Au@MFNC were in pure PBS (1/15 M, pH 7.4) (curve d and e). The results showed that Au@MFNC could not directly react with Pd@Z8P to realize the amplification of ECL signals. Secondly, the verification of the above inferences was continued by cyclic voltammetry (CV). In Fig. 5B, Pd@Z8P as a reference (− 1.07 V), the reduction peak potential of $S_2O_8^{2-}$ shifted positively (− 0.92 V to − 0.64 V) with the change of modifying materials, indicating that the prepared catalysts greatly facilitated the reduction of $S_2O_8^{2-}$ and accelerated the ECL response between Pd@ZIF-8 and $SO_4^{\bullet-}$. It was not difficult to find that the corresponding peak currents also gradually increase, which was attributed to the decrease of the reaction potential barrier, the acceleration of the electron transport process. To make the demonstration process more convincing, the CV behaviors of Pd@Z8P and Pd@Z8P + Au@MFNC were tested in pure PBS (1/15 M, pH 7.4), and the peak currents were significantly reduced, and there was no difference between the CV curves. To further verify the amplification mechanism (Fig. 5C), we investigated the ECL spectra of Pd@Z8P, Pd@Z8P/FNC and Pd@Z8P + Au@MFNC, the corresponding ECL intensity was gradually enhanced. Also, the peak shapes and the highest peak position (559 nm) of the three remained consistent. In addition, we analyzed Au@MFNC using electron paramagnetic resonance (EPR) (Fig. S10), and in the presence of Au@MFNC and $K_2S_2O_8$, the free radicals in the system

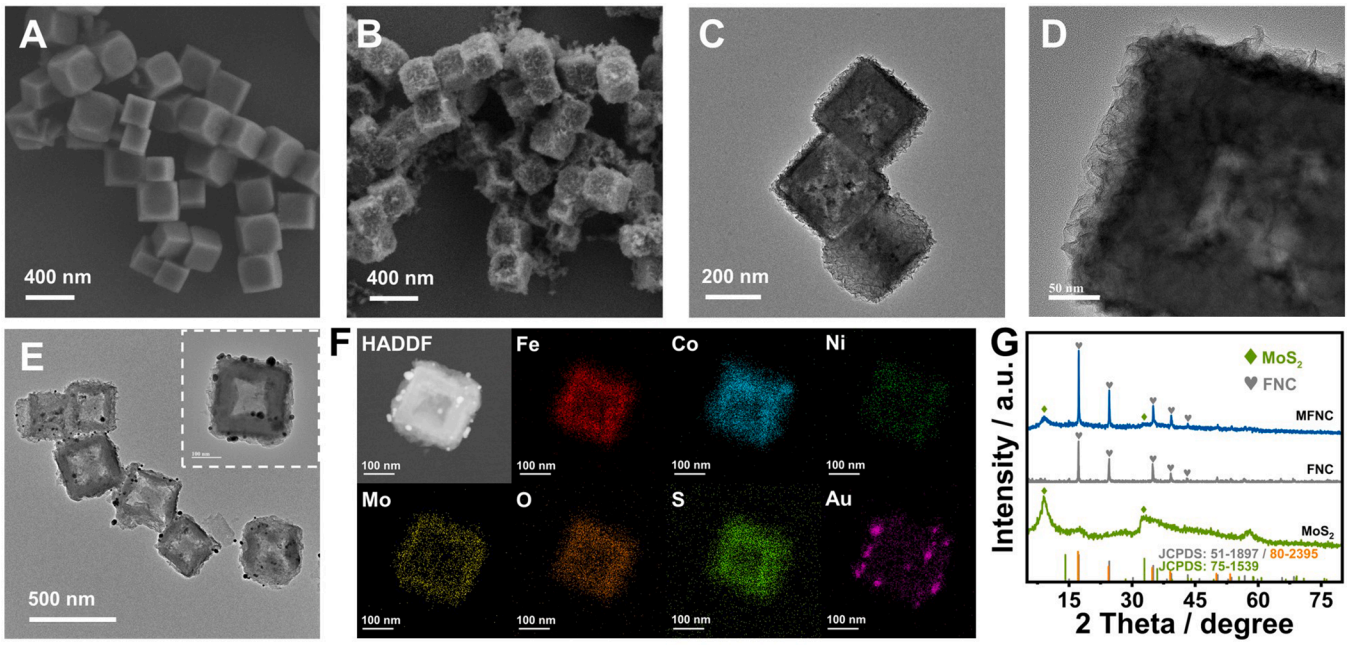

Fig. 4. (A) SEM images of FNC and (B) MFNC. (C-D) TEM images of MFNC, and (E) Au@MFNC. (F) TEM-EDS elemental mappings of Au@MFNC. (G) XRD patterns of MoS_2, FNC and MFNC.

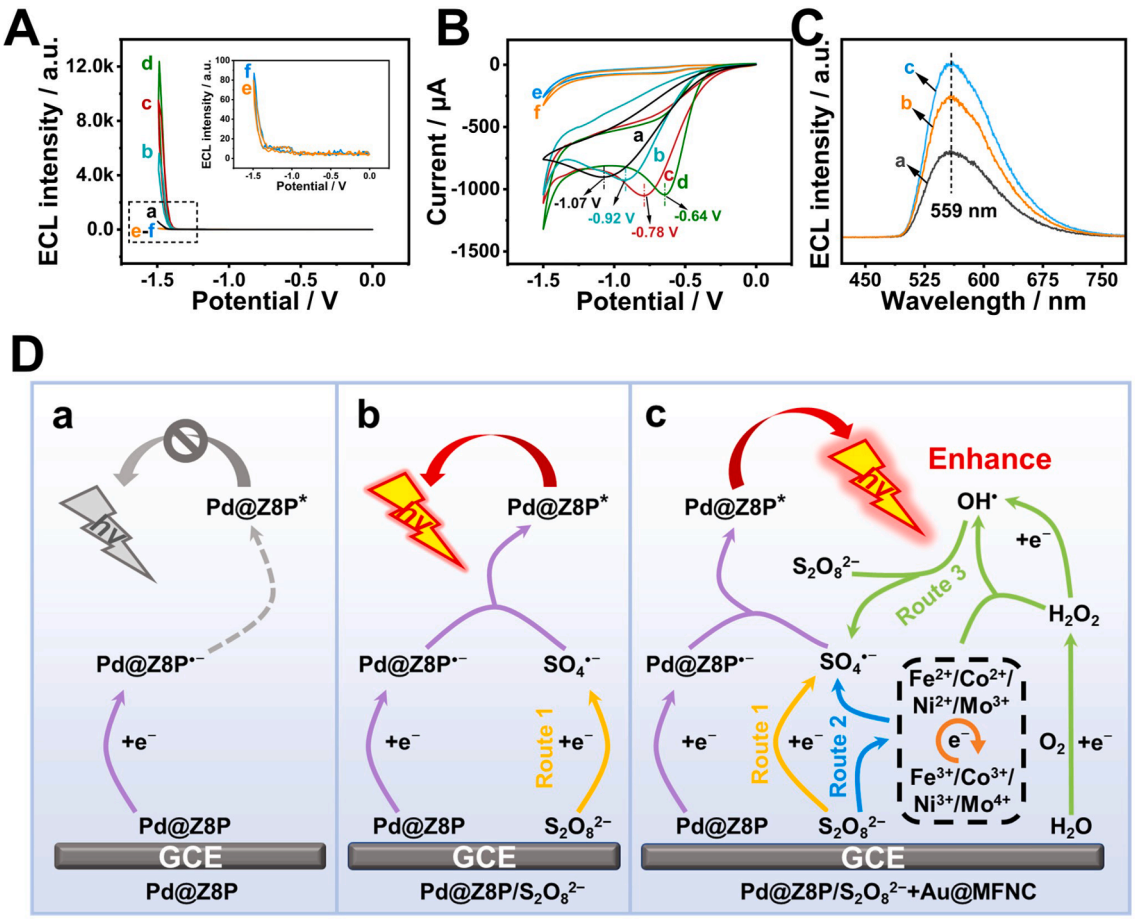

Fig. 5. (A) ECL responses and (B) CV curves of bare GCE (a), Pd@Z8P (b), Pd@Z8P/FNC (c) and Pd@Z8P + Au@MFNC (d) in PBS (1/15 M, pH 7.4 with 74.65 mM $S_2O_8^{2-}$), and Pd@Z8P (e) and Pd@Z8P + Au@MFNC (f) in pure PBS (1/15 M, pH 7.4). (C) ECL emission spectra of Pd@Z8P (a), Pd@Z8P + FNC (b) and Pd@Z8P + Au@MFNC (c) in PBS (1/15 M, pH 7.4 with 74.65 mM $S_2O_8^{2-}$). (D) Schematic diagram of possible ECL mechanism.

were captured with 5,5-dimethyl-1-pyrroline *N*-oxide (DMPO), and it was clear that both $SO_4^{\bullet-}$ and $OH^{\bullet}$ were present, successfully validating the proposed co-reaction-enhancing mechanism for Au@MFNC. Finally, we plotted two operating curves, Ab_2-Pd@Z8P/CA19-9/BSA/Ab_1/Au@MFNC/GCE (curve a) and Ab_2-Pd@Z8P/CA19-9/BSA/Ab_1/FNC/GCE (curve b), to demonstrate that the prepared immunosensors have high sensitivity. In Fig. S11, both operating curves have a good linear relationship, and the sensor shown in curve a is an ECL immunosensor in the presence of Au@MFNC, while curve b is an ECL immunosensor in the presence of FNC. The sensitivity of the immunosensors can be compared by the slopes of the linear equations of the two curves, and it is clear that the slopes of the curves decrease gradually from curve a to curve b, indicating that the constructed immunosensors have the optimal sensitivity. Based on the above results, the ECL signals of the Pd@Z8P were significantly improved indirectly by Au@MFNC and enhanced the sensitivity of the sensor.

3.6. Possible ECL mechanism

The possible ECL mechanism for the Pd@Z8P/$S_2O_8^{2-}$/Au@MFNC system was shown in Fig. 5D. Firstly, Pd@Z8P had no ECL signal in pure PBS (1/15 M, pH 7.4) (Fig. 5D, a). Then, when the $S_2O_8^{2-}$ was added, a small amount of $SO_4^{\bullet-}$ was aggregated near the luminophores, exhibiting tenuous ECL signal (Fig. 5D, b). Finally, Au@MFNC were further added to the system, and the ECL signal was enhanced (Fig. 5D, c). The specific mechanism was as follows: In route 1, a small number of $S_2O_8^{2-}$ gained electrons to produce $SO_4^{\bullet-}$ (Eq. (1)), which reacted with Pd@Z8P to produce a low ECL signal. In route 2, Fe^{3+}, Ni^{3+}, Co^{3+}, and Mo^{4+} captured electrons for conversion to the lower valence state, which accelerated the catalytic $S_2O_8^{2-}$ and consistently produced of a large amount of $SO_4^{\bullet-}$ (Eqs. (2)–(3)), enhancing the ECL signals and realizing a reversible transition of the valence state of the metal ions. In route 3, $OH^{\bullet}$ was formed by reacting variable valence metal ions with H_2O_2 (Eqs. (4)–(5)), and further reacted with $S_2O_8^{2-}$ to generate more $SO_4^{\bullet-}$ (Eq. (6)), achieving superimposed amplification of ECL signals. In the ECL emission route, the ground state Pd@Z8P first gained electrons to become Pd@Z8P$^{\bullet-}$ (Eq. (7)), which subsequently reacted with $S_2O_8^{2-}$ to produce the excited state (Pd@Z8P*) (Eq. (8)). Finally, Pd@Z8P* produced ECL emission and returned to Pd@Z8P (Eq. (9)), and the corresponding mechanism equation was as follows:

Route 1:

$$S_2O_8^{2-} + e^- \rightarrow SO_4^{\bullet-} + SO_4^{2-} \quad (1)$$

Route 2:

$$Fe^{3+}/Ni^{3+}/Co^{3+}/Mo^{4+} + 4e^- \rightarrow Fe^{2+}/Ni^{2+}/Co^{2+}/Mo^{3+} \quad (2)$$

$$Fe^{2+}/Ni^{2+}/Co^{2+}/Mo^{3+} + S_2O_8^{2-} \rightarrow Fe^{3+}/Ni^{3+}/Co^{3+}/Mo^{4+} + SO_4^{2-} + SO_4^{\bullet-}\ (\text{more}) \quad (3)$$

Route 3:

$$O_2 + 2H_2O + 2e^- \rightarrow H_2O_2 + 2OH^- \quad (4)$$

$$Fe^{2+}/Ni^{2+}/Co^{2+}/Mo^{3+} + H_2O_2 \rightarrow Fe^{3+}/Ni^{3+}/Co^{3+}/Mo^{4+} + OH^- + OH^{\bullet} \quad (5)$$

$$OH^{\bullet} + S_2O_8^{2-} \rightarrow O_2 + HSO_4^- + SO_4^{\bullet-}\ (\text{more}) \quad (6)$$

ECL emission:

$$Pd@Z8P + e^- \rightarrow Pd@Z8P^{\bullet -} \quad (7)$$

$$Pd@Z8P^{\bullet -} + SO_4^{\bullet -} \rightarrow Pd@Z8P^* + SO_4^{2-} \quad (8)$$

$$Pd@Z8P^* \rightarrow Pd@Z8P + h\nu \quad (9)$$

3.7. Optimization of conditions

To obtain the best performing ECL immunosensor, we optimized the key influencing factors of the ECL signal. In this work, we used the Box-Behnken Design for experimental conditions optimization via response surface analysis to explore factor interactions and determine the best combination of conditions. In Fig. 6, the substrate (Au@MFNC) concentration (1.0 − 5.0 mg/mL), pH (7.0 − 7.8), and $S_2O_8^{2-}$ concentration (50.0 − 100.0 mM) were identified as the optimized ranges after the initial screening. The data were analyzed using the Design-Expert software and the equations for the response surface were simulated as: $I = -1288280 + 340523A + 952.02B + 4000.57C - 6.09AB + 170.50AC - 0.26BC - 23009.13A^2 - 6.07B^2 - 877.60C^2$ (I: ECL intensity; A: pH; B: $S_2O_8^{2-}$ concentration; C: substrate concentration). Finally, we obtained the optimal conditions as follows: when A was 7.4, B was 74.65 mM and C was 3.0 mg/mL, the strongest ECL signal (13334.6 a.u.) was obtained. By optimizing the above experimental conditions, we aimed to ensure that the constructed immunosensor achieved optimal performance in subsequent ECL detection.

3.8. Detection performance of ECL immunosensor for CA19-9

Under optimum experimental conditions, we tested a range of different concentrations of CA19-9 using the constructed immunosensor. In Fig. 7A, as the CA19-9 concentration increased from 1×10^{-4} U/mL to 1×10^{2} U/mL, the corresponding ECL signal was enhanced. Fig. 7B reflected the log-linear relationship between ECL intensity and CA19-9 concentration, which provided a good linear regression equation: $I = 9077.76 + 1440.04 \lg c$, correlation coefficient (R^2) was 0.996 (I: ECL intensity; c: CA19-9 concentration). The limit of detection (LOD) of 6×10^{-5} U/mL (S/N = 3) was obtained by theoretical calculations, and the sensor had a much lower LOD and achieved an ultrasensitive detection of CA19-9 compared with previously published literature (Table. S2). Moreover, the constructed ECL immunosensor exhibited excellent performance. Firstly, to investigate the operating stability of the constructed ECL immunosensor (Fig. 7C), the detection of CA19-9 (100 U/mL) over 11 scan cycles showed a relative standard deviation (RSD) of only 1.24%. In addition, we tested the ECL intensity of the immunosensor stored at 4 °C for 7 consecutive days (Fig. S12), showing favorable storage stability. Secondly, in Fig. 7D, four common tumor markers, CEA, NSE, CA15-3 and CD44, were used as interferences. The constructed immunosensor had essentially no ECL response when 10 U/mL interferences alone were detected. Two samples with different concentrations of CA19-9 (1 U/mL and 10 U/mL) were added to high concentrations of interferences (10 U/mL and 100 U/mL) for mixed detection, and RSD results of 4.34% and 4.38% were obtained, which were consistent with the ECL signals when CA19-9 was detected alone. The above results indicated that the immunosensor had satisfactory selectivity. Finally, the repeatability of the immunosensor was evaluated by intra-batch and inter-batch precision. In Fig. 7E and F, the RSDs of intra- and inter-batch precision of 2.07% and 1.66%, respectively, were obtained for the detection of 50 U/mL CA19-9.

3.9. Sample analysis

To evaluate the practicality of the proposed ECL immunosensor in clinical medicine. We selected human serum containing CA19-9 as the original sample and applied the sensor to detect CA19-9 in human serum samples using the standard addition method. Firstly, the serum sample was centrifuged to remove the macromolecular matrix and to obtain the supernatant. Subsequently, standard samples of different concentrations were added dropwise to serum samples for detection (5 times/sample). Secondly, the calculation results were shown in Table 1, with recoveries of 99.0 − 102.4% and RSD of 1.2 − 3.1%, showing good precision and accuracy. Finally, to further confirm that the proposed immunosensor can be used to identify CA19-9 in real samples, we used an enzyme-linked immunosorbent assay (ELISA) kit as a control and evaluated the precision and accuracy of the two assays using F-test and t-test [41–43]. The results are shown in Table S1, where the calculated F-test value was lower than the critical value ($F_{0.95} = 6.39$), indicating that there was no significant difference between the two analytical methods. Meanwhile, the t-test result was also lower than the critical value ($t_{0.05} = 2.78$). In conclusion, the proposed ECL immunosensor was fully validated to have the ability to clinically detect CA19-9.

4. Conclusion

To sum up, we propose a co-assembly strategy involving PTCA coordination in ZIF-8, which first attenuated the ACQ effect of PAHs. Then, a co-reaction accelerator (Au@MFNC) nanocomposite was designed to achieve the re-amplification of the ECL signal of Pd@Z8P. By virtue of the excellent redox properties of the variable valence metals, the catalytic reduction of $S_2O_8^{2-}$ was accelerated to satisfy the large number of reactive intermediates necessary for ECL immunosensors. Finally, the constructed immunosensor showed a wide detection range ($1 \times 10^{-4} - 1 \times 10^{2}$ U/mL) and a LOD as low as 6×10^{-5} U/mL in the detection of CA19-9 with good selectivity, repeatability and stability. It also provided potential application value in the early diagnosis as well as treatment of PC, and opened up new horizons for the preparation of high-performance ECL immunosensors.

CRediT authorship contribution statement

Haiyang Li: Writing – original draft, Data curation, Conceptualization. **Mingyue Shao:** Methodology, Data curation. **Jinglong Fang:** Software, Investigation. **Yuyang Li:** Methodology. **Xiaojun Sun:** Data

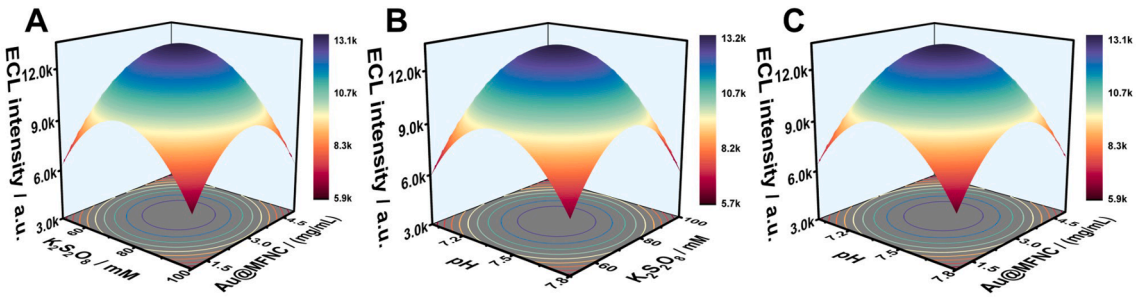

Fig. 6. (A-C) Optimization of $S_2O_8^{2-}$ concentration, pH and Au@MFNC concentration.

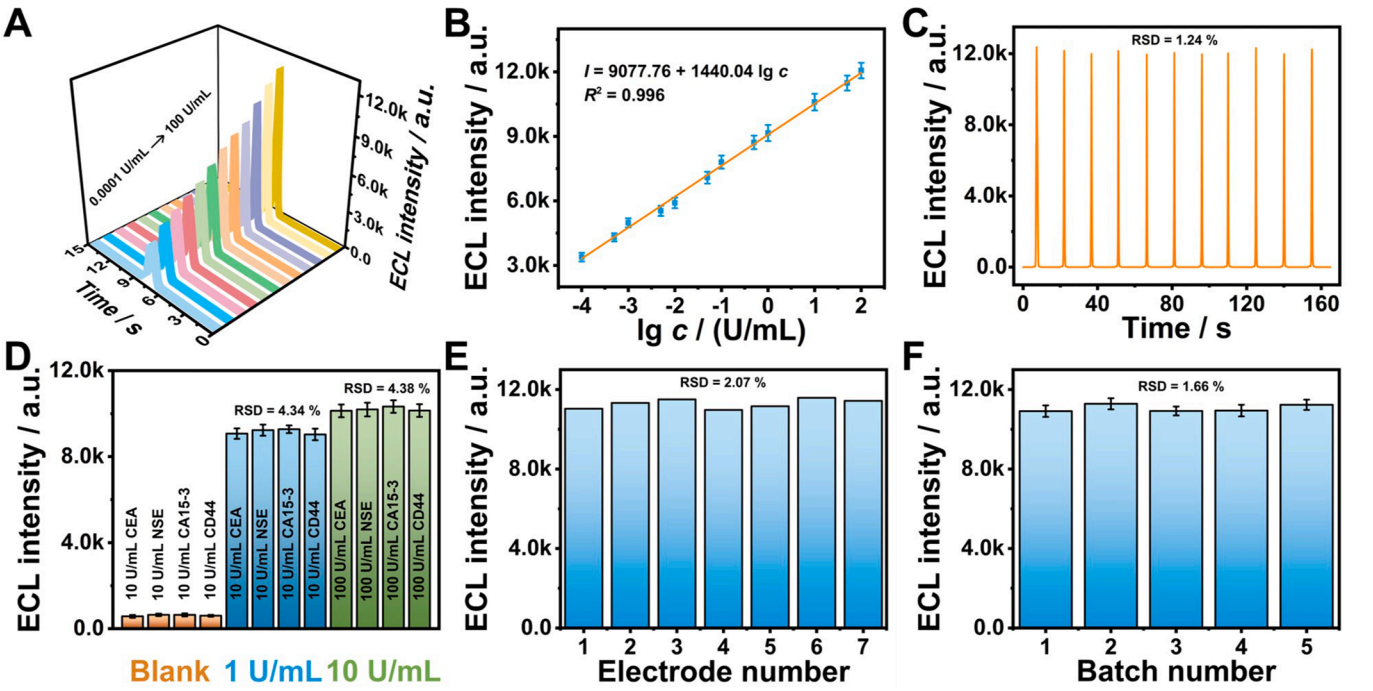

Fig. 7. (A) ECL responses for different CA19-9 concentrations (1×10^{-4} U/mL to 1×10^{2} U/mL) and (B) corresponding calibration curve. (C) Operation stability, (D) selectivity and (E-F) repeatability.

Table 1
The ECL immunosensor applied in real samples.

Sample (U/mL)	Addition content (U/mL)	Average (U/mL ± SD, $n = 5$)	RSD (%)	Recovery (%)
3.32	0.85	4.19 ± 0.032	3.1	102.4
	3.15	6.44 ± 0.063	1.2	99.0
	5.20	8.60 ± 0.027	2.0	101.5

curation. **Xiang Ren:** Project administration, Formal analysis. **Qin Wei:** Resources, Methodology. **Huangxian Ju:** Software, Resources. **Hongmin Ma:** Writing – review & editing, Funding acquisition.

Declaration of competing interest

The authors declare that they have no known competing financial interests or personal relationships that could have appeared to influence the work reported in this paper.

Data availability

No data was used for the research described in the article.

Acknowledgements

This work was financially supported by the National Natural Science Foundation of China (22374059), Wei and Ma thank the Young Taishan Scholars Program of Shandong Province of China.

Appendix A. Supplementary data

Supplementary data to this article can be found online at https://doi.org/10.1016/j.cej.2024.153315.

References

[1] H. Qi, Z. Wang, H. Li, F. Li, Directionally in situ self−assembled iridium(iii)−polyimine complex−encapsulated metal-organic framework two−dimensional nanosheet electrode to boost electrochemiluminescence sensing, Anal. Chem. 95 (2023) 12024–12031, https://doi.org/10.1021/acs.analchem.3c01882.
[2] Z. Xing, X. Gou, L.P. Jiang, J.J. Zhu, C. Ma, An in situ investigation of the protein corona formation kinetics of single nanomedicine carriers by self-regulated electrochemiluminescence microscopy, Angew. Chem. Int. Ed. 62 (2023) e202308950, https://doi.org/10.1002/anie.202308950.
[3] H. Gao, J. Zhang, Y. Liu, W. Tu, T. Wei, Z. Dai, Triple−helix molecular switch electrochemiluminescence nanoamplifier based on a S−doped Lu_2O_3/Ag_2S pair for sensitive microrna detection, Anal. Chem. 91 (2019) 12038–12045, https://doi.org/10.1021/acs.analchem.9b03071.
[4] F. Yin, Q. Sun, X. Huang, G. Wu, Y. Zhang, Y. Shen, Recent progress in signal enhancement of nanomaterials−based electrochemiluminescence systems, TrAC Trends Anal. Chem. 169 (2023) 117376, https://doi.org/10.1016/j.trac.2023.117376.
[5] L. Liu, Y. Xu, Y. Zhu, H. Wang, Y. Chai, R. Yuan, Near-infrared electrochemiluminescence of carbon nitride quantum dots for ultrasensitive microRNA assay, Chem. Eng. J. 472 (2023) 145107, https://doi.org/10.1016/j.cej.2023.145107.
[6] X. Zhang, P. Wang, Y. Nie, Q. Ma, Recent development of organic nanoemitter-based ECL sensing application, TrAC Trends Anal. Chem. 143 (2021) 116401, https://doi.org/10.1016/j.trac.2021.116410.
[7] E. Sobhanie, F. Salehnia, G. Xu, Y. Hamidipanah, S. Arshian, A. Firoozbakhtian, et al., Recent trends and advancements in electrochemiluminescence biosensors for human virus detection, TrAC Trends Anal. Chem. 157 (2022) 116727, https://doi.org/10.1016/j.trac.2022.116727.
[8] Y. Zhao, L. Bouffier, G. Xu, G. Loget, N. Sojic, Electrochemiluminescence with semiconductor (nano)materials, Chem. Sci. 13 (2022) 2528–2550, https://doi.org/10.1039/d1sc06987j.
[9] D. Lai, Z. Mu, J. Zuo, J. Zhou, Q. Zhang, K. Chen, et al., Perylene−based electrochemiluminescent metal-organic frameworks for detection of zearalenone, ACS Appl. Nano Mater. 6 (2023) 22416–22425, https://doi.org/10.1021/acsanm.3c04704.
[10] J.-M. Wang, L.-Y. Yao, W. Huang, Y. Yang, W.-B. Liang, R. Yuan, et al., Overcoming aggregation−induced quenching by metal−organic framework for electrochemiluminescence (ECL) enhancement: Zn−PTC as a new ECL emitter for ultrasensitive microRNAs detection, ACS Appl. Mater. Interfaces 13 (2021) 44079–44085, https://doi.org/10.1021/acsami.1c13086.
[11] Y. Hong, J.W.Y. Lam, B.Z. Tang, Aggregation−induced emission, Chem. Soc. Rev. 40 (2011) 5361–5388, https://doi.org/10.1039/c1cs15113d.
[12] Y. Wu, Z. Mu, F. Gong, M. Qing, J. Zhou, K. Chen, et al., Overcoming aggregation−caused quenching by an improved porphyrin hybrid and its application in enhanced electrochemiluminescence biosensing, ACS Sustainable Chem. Eng. 11 (2023) 14124–14132, https://doi.org/10.1021/acssuschemeng.3c03608.
[13] L. Jiao, J.Y.R. Seow, W.S. Skinner, Z.U. Wang, H.-L. Jiang, Metal–organic frameworks: structures and functional applications, Mater. Today 27 (2019) 43–68, https://doi.org/10.1016/j.mattod.2018.10.038.
[14] Z. Wang, X. Jiang, R. Yuan, Y. Chai, N−(aminobutyl)−N−(ethylisoluminol) functionalized Fe−based metal−organic frameworks with intrinsic mimic

peroxidase activity for sensitive electrochemiluminescence mucin1 determination, Biosens. Bioelectron. 121 (2018) 250–256, https://doi.org/10.1016/j.bios.2018.09.022.
[15] W. Li, Y. Li, L.-D. Zhao, R. Yuan, Y. Zhuo, X. Zhong, Triple−helix as a target converter for trace pesticide detection based on CRISPR/Cas12a−based ECL biosensor, Sens. Actuators, B 409 (2024) 135599, https://doi.org/10.1016/j.snb.2024.135599.
[16] L. Zheng, Q. Guo, C. Yang, J. Wang, X. Xu, G. Nie, Electrochemiluminescence and photoelectrochemistry dual−signal immunosensor based on $Ru(bpy)_3^{2+}$−functionalized MOF for prostate−specific antigen sensitive detection, Sens. Actuators, B 379 (2023) 133269, https://doi.org/10.1016/j.snb.2022.133269.
[17] J. Xu, W. Yang, J. Ni, Q. Wang, Z. Lin, Co−reactant confined and vertically ordered silica nanochannel regulated electrochemiluminescence for homogeneous detection of miRNA, Sens. Actuators, B 397 (2023) 134694, https://doi.org/10.1016/j.snb.2023.134694.
[18] M.-N. Ma, Y. Zhuo, R. Yuan, Y.-Q. Chai, New Signal Amplification strategy using semicarbazide as Co−reaction accelerator for highly sensitive electrochemiluminescent aptasensor construction, Anal. Chem. 87 (2015) 11389–113897, https://doi.org/10.1021/acs.analchem.5b02848.
[19] X. Song, X. Ren, W. Zhao, L. Zhao, S. Wang, C. Luo, et al., A portable microfluidic−based electrochemiluminescence sensor for trace detection of trenbolone in natural water, Anal. Chem. 94 (2022) 12531–12537, https://doi.org/10.1021/acs.analchem.2c02780.
[20] H. Li, L. Dai, Q. Huang, J. Song, L. Liu, Y. Li, et al., FeNi−MIL−88B−based electrochemiluminescence immunosensor for ultra−sensitive detection of CD44 protein via dual−quenching strategy, Anal. Chim. Acta 1303 (2024) 342520, https://doi.org/10.1016/j.aca.2024.342520.
[21] Q. Wu, P. Wang, X. Yang, M. Wei, M. Zhou, Y. Pu, et al., Fe−Co−Co prussian blue analogues as a novel co−reaction accelerator for ultrasensitive electrochemiluminescent biosensor construction, Sens. Actuators, B 297 (2019) 126767, https://doi.org/10.1016/j.snb.2019.126767.
[22] D.K. Owens, K.W. Davidson, A.H. Krist, M.J. Barry, M. Cabana, A.B. Caughey, et al., Screening for pancreatic cancer, JAMA 322 (2019) 438–444, https://doi.org/10.1001/jama.2019.10232.
[23] T. Kamisawa, L.D. Wood, T. Itoi, K. Takaori, Pancreatic cancer, Lancet 388 (2016) 73–85, https://doi.org/10.1016/s0140−6736(16)00141−0.
[24] G. Luo, K. Jin, S. Deng, H. Cheng, Z. Fan, Y. Gong, et al., Roles of CA19−9 in pancreatic cancer: biomarker, predictor and promoter, Biochim. Biophys. Acta, Rev. Cancer 1875 (2021) 188409, https://doi.org/10.1016/j.bbcan.2020.188409.
[25] K. Luo, C. Zhao, Y. Luo, C. Pan, J. Li, Electrochemical sensor for the simultaneous detection of CA72−4 and CA19−9 tumor markers using dual recognition via glycosyl imprinting and lectin−specific binding for accurate diagnosis of gastric cancer, Biosens. Bioelectron. 216 (2022) 114672, https://doi.org/10.1016/j.bios.2022.114672.
[26] J. Wang, L. Zhuo, P. Zhao, W. Liao, H. Wei, Y. Yang, et al., Screening for a 177Lu−labeled CA19–9 monoclonal antibody via PET imaging for colorectal cancer therapy, Chin. Chem. Lett. 33 (2022) 3502–3506, https://doi.org/10.1016/j.cclet.2022.03.056.
[27] H. Tanaka, K. Tamura, T. Abe, T. Yoshida, A. Macgregor-Das, M. Dbouk, et al., Serum carboxypeptidase activity and genotype−stratified CA19−9 to detect early−stage pancreatic cancer, Clin. Gastroenterol. Hepatol. 20 (2022) 2267–2275, https://doi.org/10.1016/j.cgh.2021.10.008.
[28] X.Y. Yu, Y. Feng, Y. Jeon, B. Guan, X.W. Lou, U. Paik, Formation of Ni–Co–MoS_2 nanoboxes with enhanced electrocatalytic activity for hydrogen evolution, Adv. Mater. 28 (2016) 9006–9011, https://doi.org/10.1002/adma.201601188.
[29] W. Morris, C.J. Stevens, R.E. Taylor, C. Dybowski, O.M. Yaghi, M. A. Garcia−Garibay, NMR and X−ray study revealing the rigidity of zeolitic imidazolate frameworks, J. Phys. Chem. C 116 (2012) 13307–13312, https://doi.org/10.1021/jp303907p.
[30] S. Xiang, J. Li, M. Shi, H. Yang, R. Cai, W. Tan, A novel ECL aptasensor for ultra−highly sensitive detection of patulin based on terbium organic gels as Co−reaction accelerator in a 3, 4, 9, 10−perylenetetracarboxylic acid/$K_2S_2O_8$ system, Sens. Actuators, B 394 (2023) 134365, https://doi.org/10.1016/j.snb.2023.134365.
[31] J. Ma, W. Wang, Y. Li, Z. Lu, X. Tan, H. Han, Novel porphyrin Zr metal-organic framework (PCN−224)−based ultrastable electrochemiluminescence system for PEDV, Sensing Anal. Chem. 93 (2021) 2090–2096, https://doi.org/10.1021/acs.analchem.0c03836.
[32] X. Li, M. Xu, Z. Geng, X. Xu, X. Han, L. Chen, et al., Novel pH−responsive CaO_2@ZIF−67−HA−ADH coating that efficiently enhances the antimicrobial, osteogenic, and angiogenic properties of titanium implants, ACS Appl. Mater. Interfaces 15 (2023) 42965–42980, https://doi.org/10.1021/acsami.3c08233.
[33] X. Niu, S. Yan, R. Zhao, H. Li, X. Liu, K. Wang, Design and electrochemical chiral sensing of the robust sandwich chiral composite d−His−ZIF−8@Au@ZIF−8, ACS Appl. Mater. Interfaces 15 (2023) 22435–22444, https://doi.org/10.1021/acsami.3c03947.
[34] I. Shaukat, N. Iqbal, T. Noor, M. Raza, R. Ahmad, CoSe/NC composites through the selenization of ZIF−67 for high−performance supercapacitor electrodes, Energy Fuels 37 (2023) 16150–16159, https://doi.org/10.1021/acs.energyfuels.3c03169.
[35] Y. Li, S. Li, M. Bao, L. Zhang, C. Carraro, R. Maboudian, et al., Pd nanoclusters confined in ZIF−8 matrixes for fluorescent detection of glucose and cholesterol, ACS Appl. Nano Mater. 4 (2021) 9132–9142, https://doi.org/10.1021/acsanm.1c01712.
[36] L. Yang, Y. Jin, X. Fang, Z. Cheng, Z. Zhou, Magnetically recyclable core-shell structured Pd−based catalysts for semihydrogenation of phenylacetylene, Ind. Eng. Chem. Res. 56 (2017) 14182–14191, https://doi.org/10.1021/acs.iecr.7b03016.
[37] J. Li, H. Jia, X. Ren, Y. Li, L. Liu, R. Feng, et al., Dumbbell plate−shaped aiegen−based luminescent MOF with high quantum yield as self−enhanced ECL tags: mechanism insights and biosensing application, Small 18 (2022) 2106567, https://doi.org/10.1002/smll.202106567.
[38] Y. Guo, J. Tang, Z. Wang, Y. Sugahara, Y. Yamauchi, Hollow porous heterometallic phosphide nanocubes for enhanced electrochemical water splitting, Small 14 (2018) 1802442, https://doi.org/10.1002/smll.201802442.
[39] B. Wang, X. Zhong, Y. Chai, R. Yuan, An ECL biosensor for sensitive detection of concanavalin A based on the ECL quenching of Ru complex by MoS_2 nanoflower, Sens. Actuators, B 245 (2017) 247–255, https://doi.org/10.1016/j.snb.2017.01.180.
[40] X. Song, X. Shao, L. Dai, D. Fan, X. Ren, X. Sun, et al., Triple amplification of 3,4,9,10−perylenetetracarboxylic acid by Co^{2+}−based metal-organic frameworks and silver-cysteine and its potential application for ultrasensitive assay of procalcitonin, ACS Appl. Mater. Interfaces 12 (2020) 9098–9106, https://doi.org/10.1021/acsami.9b23248.
[41] T. Gan, Z. Wang, J. Gao, J. Sun, K. Wu, H. Wang, et al., Morphology–dependent electrochemical activity of Cu_2O polyhedrons and construction of sensor for simultaneous determination of phenolic compounds with graphene oxide as reinforcement, Sens. Actuators, B 282 (2019) 549–558, https://doi.org/10.1016/j.snb.2018.11.102.
[42] X. Yu, Y. Wang, X. Chen, K. Wu, D. Chen, M. Ma, et al., White-light-exciting layer-by-layer-assembled ZnCdHgSe quantum dots/polymerized ionic liquid hybrid film for highly sensitive photoelectrochemical immunosensing of neuron specific enolase, Anal. Chem. 87 (2015) 4237–4244, https://doi.org/10.1021/ac504456w.
[43] X. Li, Y. Du, H. Wang, H. Ma, D. Wu, X. Ren, et al., Self-supply of H_2O_2 and O_2 by hydrolyzing CaO_2 to enhance the electrochemiluminescence of luminol based on a closed bipolar electrode, Anal. Chem. 92 (2020) 12693–12709, https://doi.org/10.1021/acs.analchem.0c03170.